Supporting Information

Identifying Iodide-Ion Regulation of Early-Stage Zinc Nucleation and Growth for High-Rate Anode-Free Zinc Metal Battery

Wenchao Shi,‡[a] Zhenjun Song,‡[b] Wenwei Zhang,[a] Sitian Lian,[a] Fuzhi Huang,[a] Qinyou An,[a] and Qi Li*[c]*

[a]State Key Laboratory of Advanced Technology for Materials Synthesis and Processing, Wuhan University of Technology, Wuhan, 430070, P. R. China.

[b]School of Pharmaceutical and Materials Engineering, Taizhou University, Taizhou, 318000, P. R. China.

[c]National Energy Key Laboratory for New Hydrogen-Ammonia Energy Technologies, Foshan Xianhu Laboratory Foshan 528200, P. R. China.

E-mail: anqinyou86@whut.edu.cn; liqi1@xhlab.cn

Electrolyte Preparation

The 2 M $ZnSO_4$ electrolyte was prepared by dissolving $ZnSO_4 \cdot 7H_2O$ in deionized water. The subject electrolytes were prepared by adding different amounts of lithium iodide (LiI) (99.9%), lithium chloride (LiCl), lithium bromide (LiBr) or lithium sulfate (Li_2SO_4) into 2 M $ZnSO_4$ electrolyte, noted as LiI-$ZnSO_4$, LiCl-$ZnSO_4$, LiBr-$ZnSO_4$ and Li_2SO_4-$ZnSO_4$. The optimized concentration of LiI was 0.5 M L^{-1}.

Characterization

The crystal structures of the materials were analyzed using X-ray diffractometer. The samples were also subjected to field-emission scanning electron microscopy (FESEM) using a 2020 JEOL-7100F scanning electron microscope. Raman spectra and attenuated total reflection Fourier transform infrared (ATR-FTIR) spectra were recorded using a micro-Raman spectroscopy system (Renishaw INVIA). Nuclear magnetic resonance (NMR) spectra were obtained on a Bruker Avance II 300MHz NMR spectrometer. X-ray photoelectron spectroscopy (XPS) results were obtained through a VG MultiLab 2000 instrument. Transmission electron microscopy (TEM) and the energy dispersive X-ray spectroscopy (EDX) mapping were performed on a JEM-2100F transmission electron microscope at 200 kV.

Electrochemical characterization

The electrochemical workstation (CHI660E, China) was used to test the Tafel curves between −0.1 and 0.1 V at 5 mV s^{-1}, with Zn||Zn symmetrical battery. The chronoamperometry (CA) curves were measured at an overpotential of −100 mV. The differential capacitance curves were measured by scanning at 1000 Hz. For the Zn||Zn symmetrical batteries, the Zn foil (20 µm) was cut into a round disk with a diameter of 10 mm, corresponding to a mass of about 8.9 mg. For the Zn||Cu asymmetrical battery, the Cu foil (100 µm) was cut into a round disk with a diameter of 16 mm or 10 mm. To prepare the AC cathodes, a slurry made up of AC, carbon black (Super P), and polytetrafluoroethylene (PTFE) at a weight ratio of 8:1:1. The full batteries were assembled with the Cu foil anodes (diameter of 16 mm) and AC cathodes (diameter of 8 mm) separated by a glass fiber separator with a diameter of 17 mm. All batteries were assembled as CR2016 coin batteries in an air atmosphere. The pouch battery was fabricated using an Al pouch film as a packaging substance. The cycling performances of the batteries were measured by the LAND and NEWARE instrument in the voltage range of 0.6 - 1.8 V. Additionally, cyclic voltammetry (CV) was performed with a voltage range of 0.6 - 1.8 V at different scan rates of 2, 5, 8, 10 and 20 mV s^{-1}, and electrochemical impedance spectroscopy (EIS) tests were conducted using an Autolab PGSTAT 302N in a frequency range of 0.01 Hz - 100 kHz.

Molecular dynamics (MD) simulations method

MD simulations were conducted using the LAMMPS package with the AMBER03 force field to investigate the electrolyte structures.[1] The TIP4P model was employed to simulate water molecules. The MD parameters for Zn^{2+}, SO_4^{2-}, Li^+, and I^- were utilized based on the built-in force field parameters. Each simulation cell consisted of 6960 H_2O molecules, 200 $ZnSO_4$ molecules, and 50 LiI molecules. Initially, NPT runs were conducted at 298 K for 500 ps to ensure system equilibrium, followed by another NVT run of 500 ps for analysis purposes. Radial distribution functions (RDFs) were calculated using the built-in module.

Density Functional Theory (DFT) Calculation method

We employed dispersion-corrected density-functional theory (DFT-D3) [2, 3] and the plane-wave method to compute the structures and energetics. The projector-augmented-wave (PAW) [4, 5] method in conjunction with the generalized gradient approximation (GGA) was used to determine the dispersion forces and energy. Perdew-Burke-Ernzerhof functional implemented in Vienna Ab Initio Simulation Package (VASP) [6-8] was adopted to compute the exchange-correlation potentials.

The Marcus charge transfer energy barrier, represented as $\Delta G_1^{\neq}$, was determined using the four-point method.[9, 10] Geometries of ground-state molecules were optimized using M06-2X density-functional [11] with 6-311++G(d,p) basis set (H, O atoms) and lanl2dz basis set (Zn, I, Cl, Br atoms) using Gaussian software. To ensure the minimum energy structures are obtained, the analysis of frequency was carried out. Focusing on the +1 and +2 electronic states, the high-precision single-point energies of the optimally solvated Zn^{2+} structure were identified to be E_1 and E_2, respectively. Simultaneously, for the optimally solvated Zn^{1+} structure under the +2 and +1 electronic states, the high-precision single-point energies were established to be E_3 and E_4 respectively. Following these calculations, $\Delta G_2^{\neq}$ was computed using the below formula:

$$\lambda^{(1)} = E_2 - E_4$$

$$\lambda^{(2)} = E_3 - E_1$$

$$\Delta G_1^{\neq} = \frac{\lambda^{(1)} + \lambda^{(2)}}{8}$$

The desolvation energy barrier, denoted as $\Delta G_2^{\neq}$, was approximated through the dissociation of a coordinated water molecule.

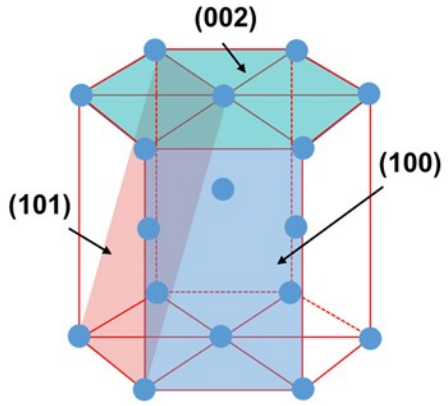

Fig. S1. The crystal structure of Zn metal.

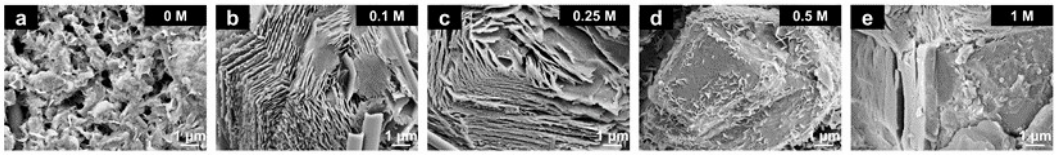

Fig. S2. SEM images of Zn plating at different concentrations of LiI additives under 10 mA cm^{-2} and 5 mAh cm^{-2}, (a) 0 M, (b) 0.1 M, (c) 0.25 M, (d) 0.5 M, (e) 1 M.

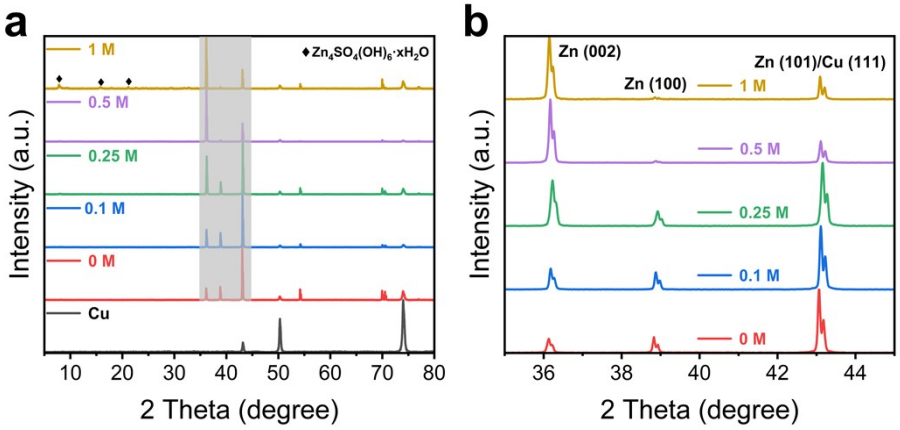

Fig. S3. (a-b) XRD patterns of Zn plating at different LiI concentrations.

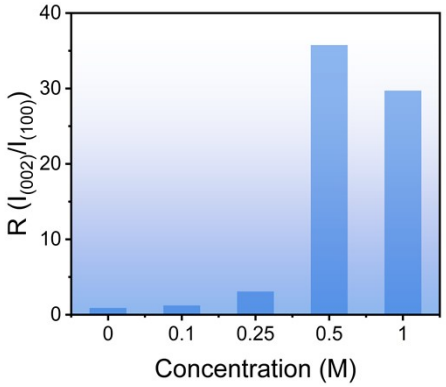

Fig. S4. The intensity ratio of diffraction peaks of Zn (002) to Zn (100) at different LiI concentrations.

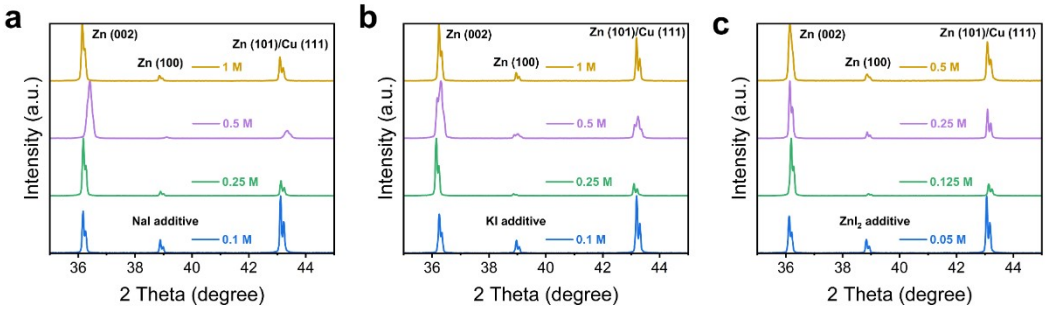

Fig. S5. XRD patterns of Zn plating with different iodide salt additives at various concentrations: (a) NaI, (b) KI, (c) ZnI_2.

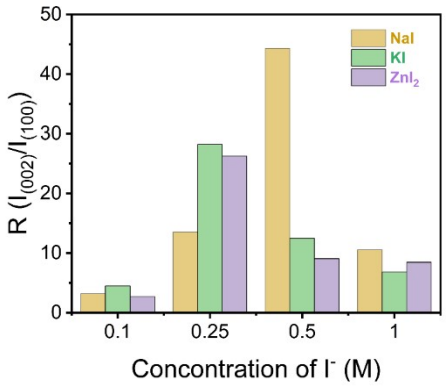

Fig. S6. The intensity ratio of the diffraction peaks of Zn (002) to Zn (100) for different iodide salt additives at various concentrations.

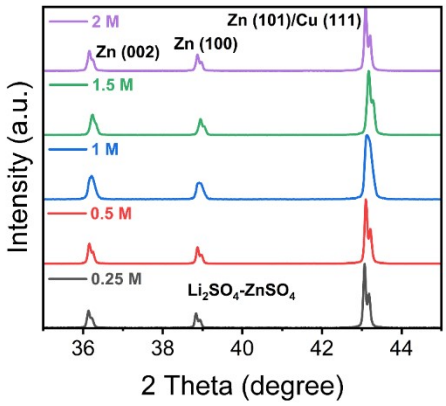

Fig. S7. (a) XRD patterns of Zn plating in the Li_2SO_4-$ZnSO_4$ electrolyte at different Li_2SO_4 concentrations.

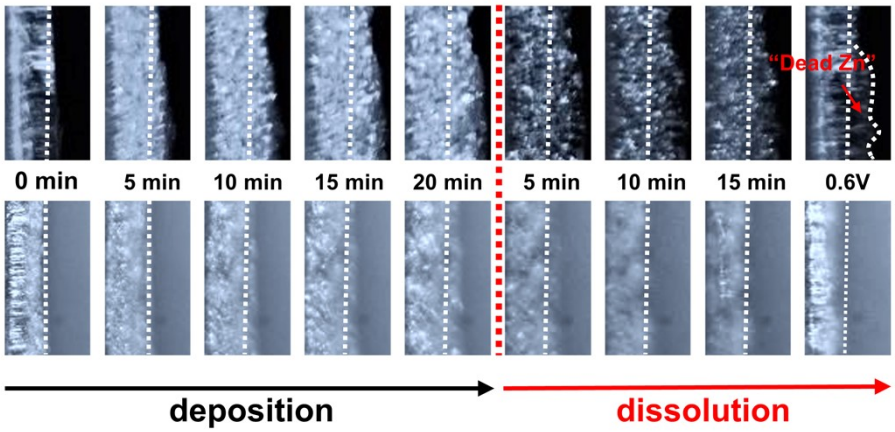

Fig. S8. In situ optical characterization of Zn deposition/dissolution process in the first cycle on Cu surfaces in the $ZnSO_4$ electrolytes with and without LiI.

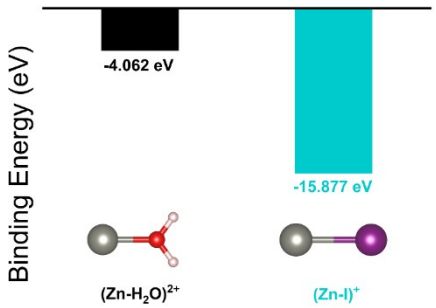

Fig. S9. The binding energies between I^-/H_2O and Zn^{2+}.

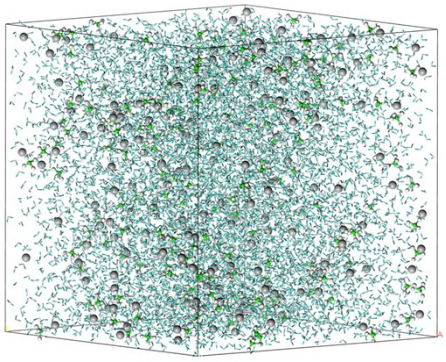

Fig. S10. The MD snapshots of $ZnSO_4$ electrolyte.

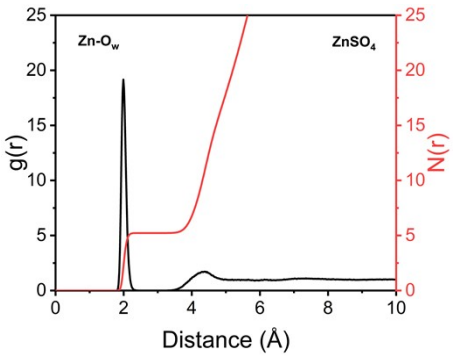

Fig. S11. RDF and the coordination number of Zn-O_w in $ZnSO_4$ electrolyte.

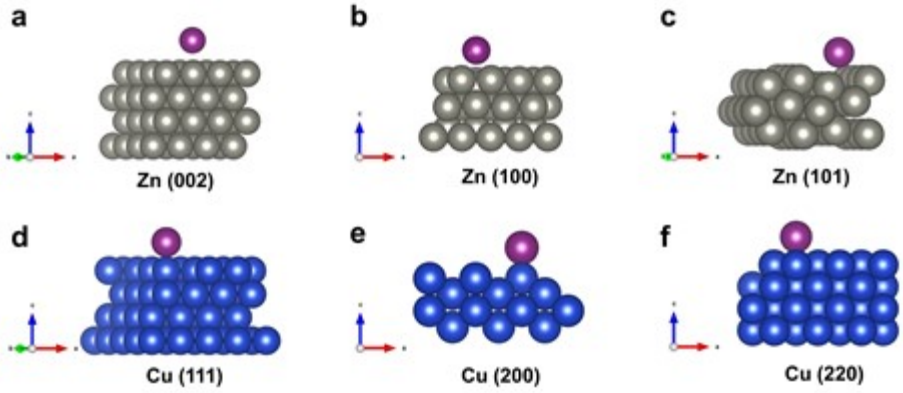

Fig. S12. (a-f) Adsorption models of I^- on different crystal planes of Zn and Cu metals.

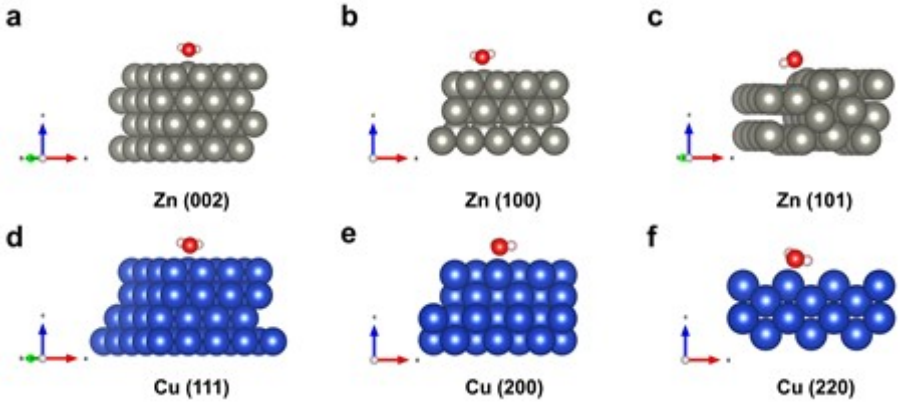

Fig. S13. (a-f) Adsorption models of water molecule on different crystal planes of Zn and Cu metals.

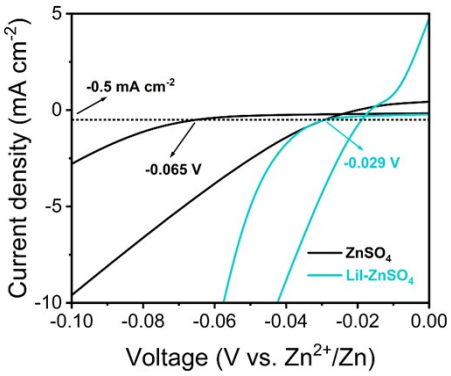

Fig. S14. Enlarged view of CV curves of Zn||Cu batteries in the electrolyte with and without LiI.

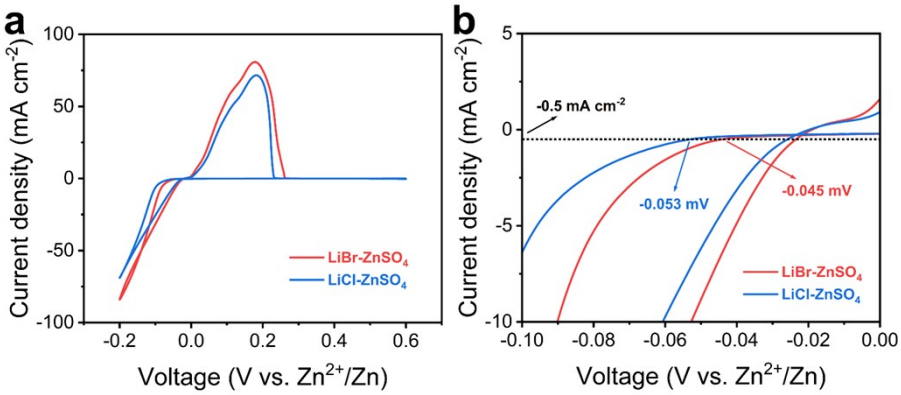

Fig. S15. (a) CV curves of Zn||Cu batteries in the electrolyte with LiCl and with LiBr. (b) Enlarged view of the corresponding CV curves.

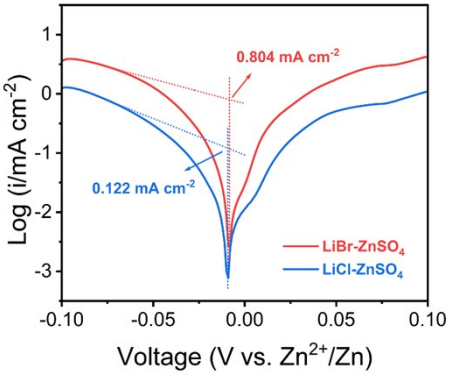

Fig. S16. Tafel curves of Zn||Zn batteries in the electrolyte with LiCl and with LiBr.

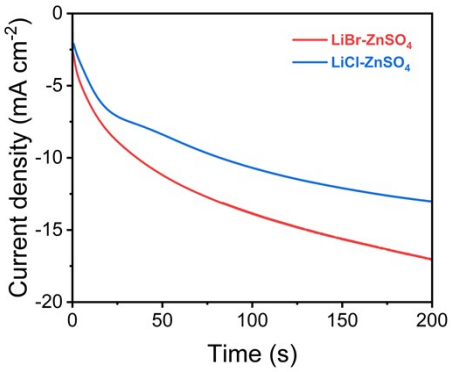

Fig. S17. CA curves of Zn||Zn batteries in the electrolyte with LiCl and with LiBr at −100 mV.

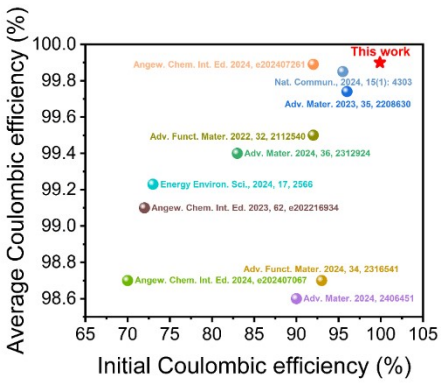

Fig. S18. Comparison of CE values with previously reported literature.[12-22]

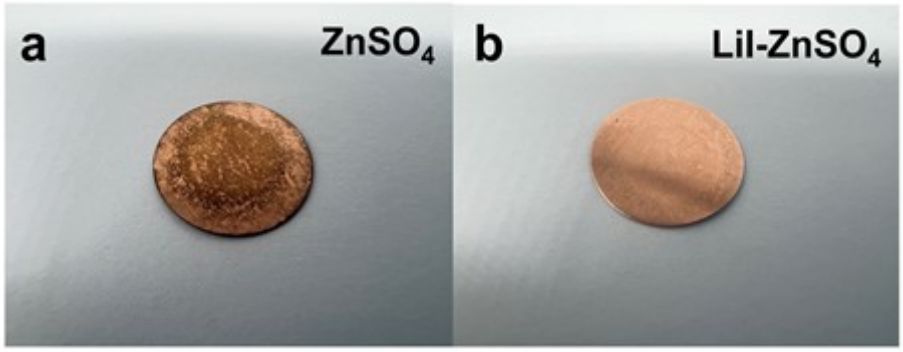

Fig. S19. (a) Optical photograph of Cu foil after 10 cycles in $ZnSO_4$ electrolyte. (b) Optical photograph of Cu foil after 10 cycles in LiI-$ZnSO_4$ electrolyte.

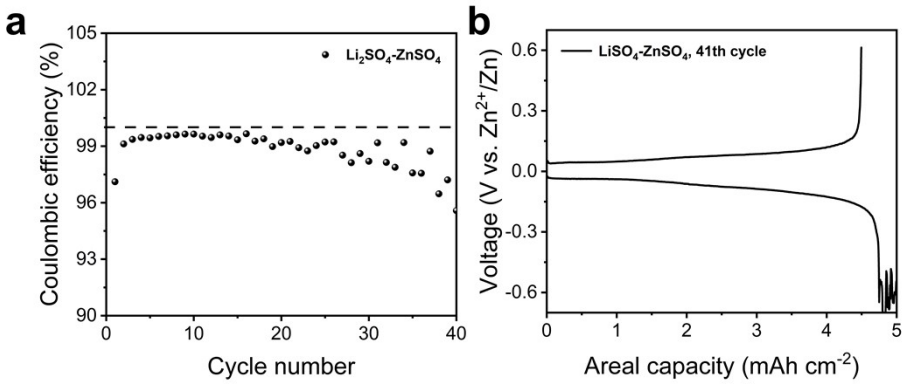

Fig. S20. (a) CE of Zn||Cu battery in the Li_2SO_4-$ZnSO_4$ electrolyte. (b) The corresponding 41th charge and discharge curve.

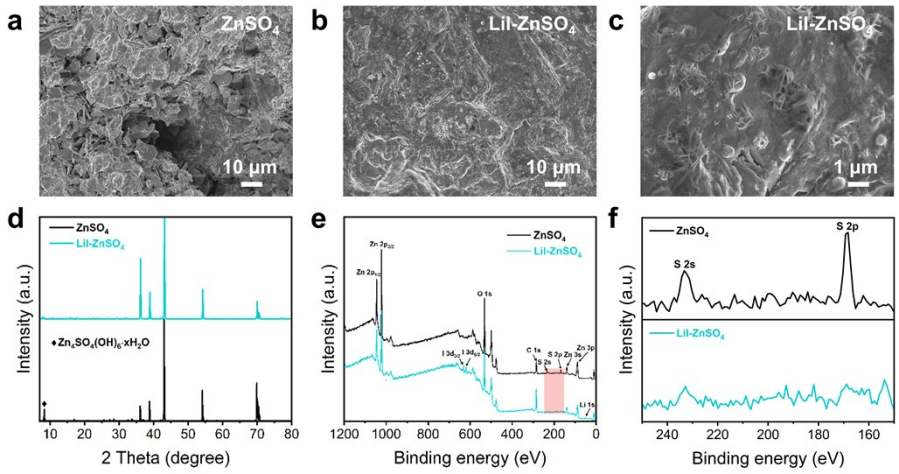

Fig. S21. Characterizations of the Zn anode after cycling in Zn symmetric cells. (a) SEM image of Zn anode in the $ZnSO_4$ electrolyte. (b-c) SEM images of Zn anode in the LiI-$ZnSO_4$ electrolyte. (d) XRD patterns of Zn anode. (e) XPS wide-scan spectra of Zn anode. (f) Enlarged XPS spectra belong to S signal.

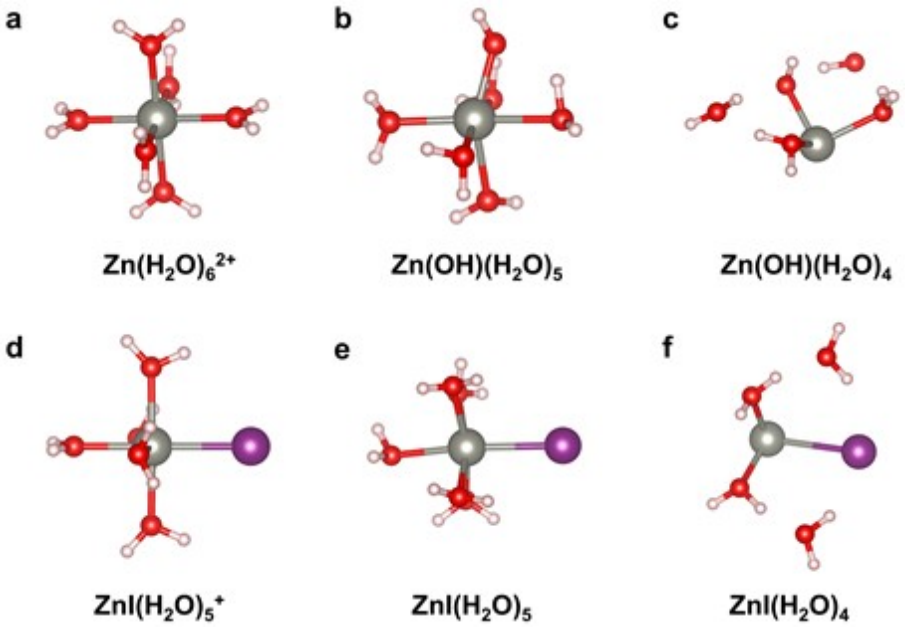

Fig. S22. The structure of key intermediates in (a-c) $ZnSO_4$ and (d-f) LiI-$ZnSO_4$ electrolytes.

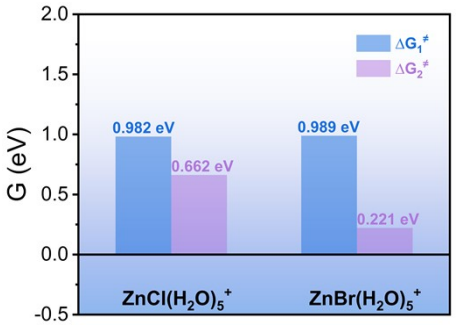

Fig. S23. The calculated Gibbs activation free energy barriers of Cl^- and Br^- coordination of the solvated Zn^{2+}.

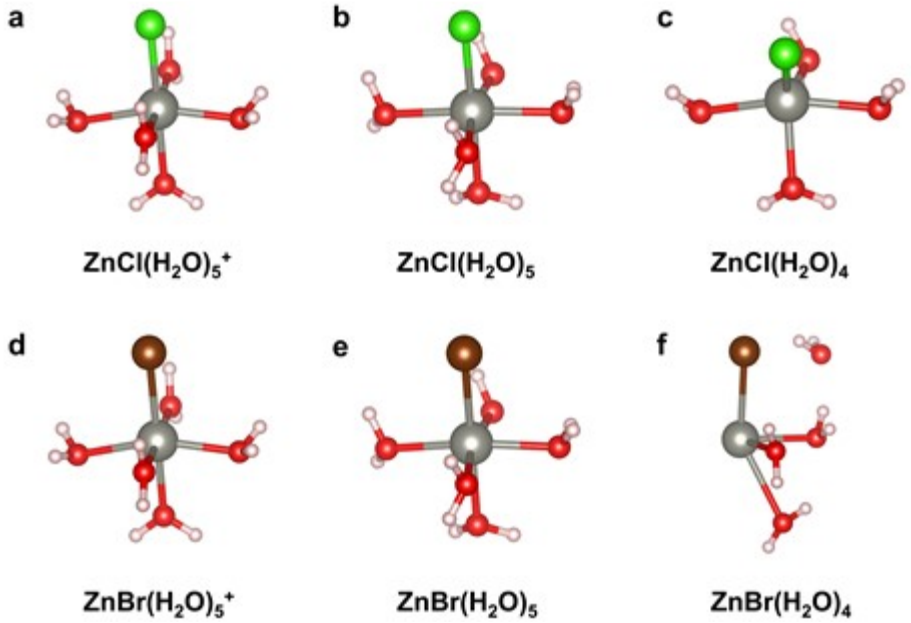

Fig. S24. The structure of key intermediates in (a-c) LiCl-$ZnSO_4$ and (d-f) LiBr-$ZnSO_4$ electrolytes.

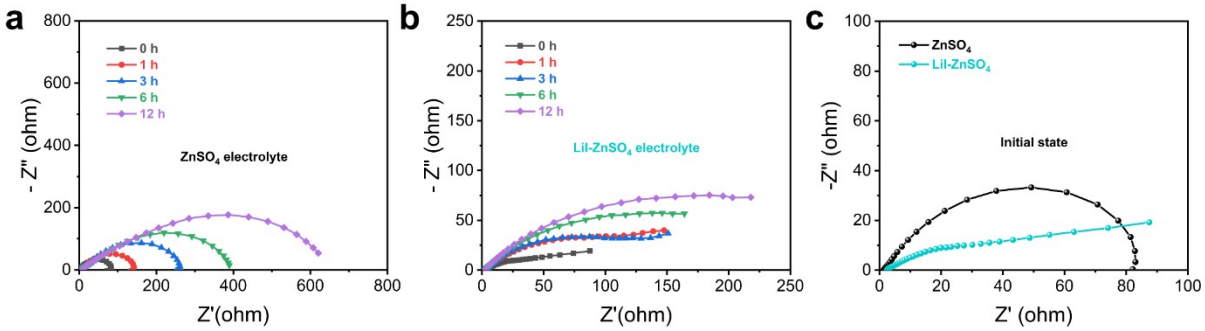

Fig. S25. EIS of Zn||Zn batteries standing for different durations in the $ZnSO_4$ electrolyte with and without LiI. (a) Zn||Zn battery in the $ZnSO_4$ electrolyte. (b) Zn||Zn battery in the LiI-$ZnSO_4$ electrolyte. (c) Zn||Zn batteries in their initial state in both electrolytes.

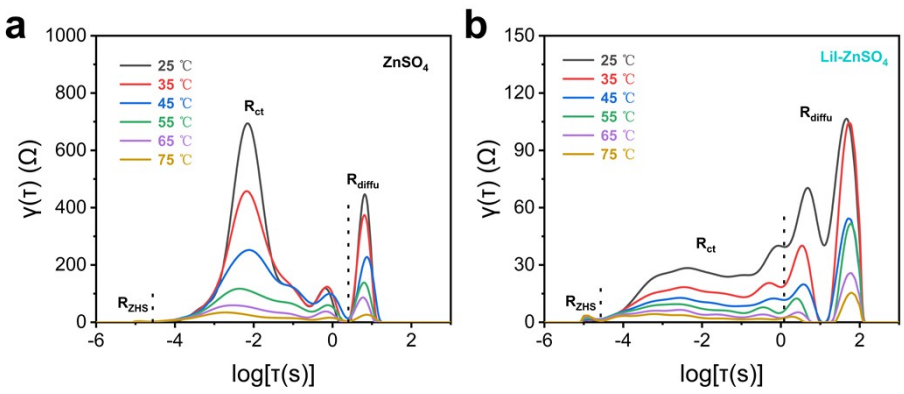

Fig. S26. DRT analysis of charge transfer process of Zn^{2+} in (a) $ZnSO_4$ and (b) LiI-$ZnSO_4$ electrolytes.

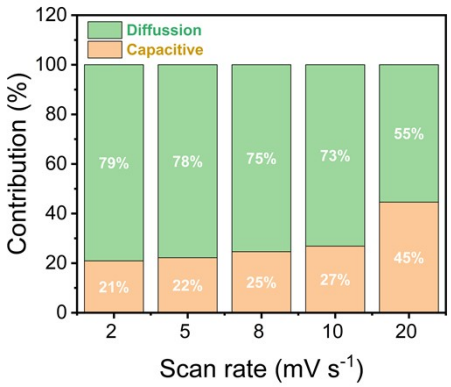

Fig. S27. The contribution ratio of capacitive processes to diffusion-controlled process at different scan rates.

The calculation of the capacity contributions from the two energy storage behaviors using the following equation:

$$i\,(V) = k_1\nu + k_2\nu^{1/2}$$

At scan rates of 2, 5, 8, 10, and 20 mV s^{-1}, the capacitive behavior contributed 21%, 22%, 25%, 27%, and 45% of the capacity, respectively.

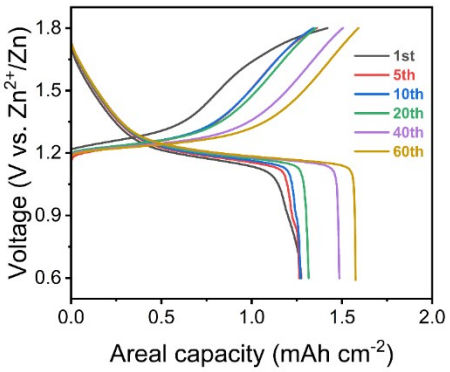

Fig. S28. The charging-discharging curves of Cu||AC batteries in LiI-$ZnSO_4$ electrolyte.

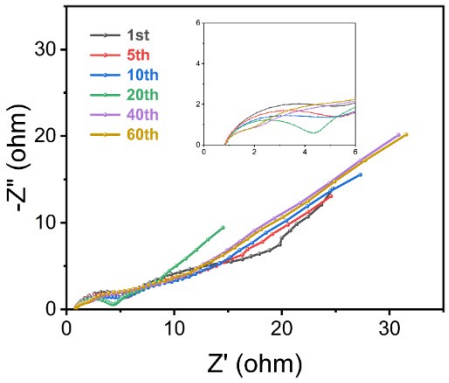

Fig. S29. EIS of Cu||AC batteries in LiI-$ZnSO_4$ electrolyte at different cycle numbers.

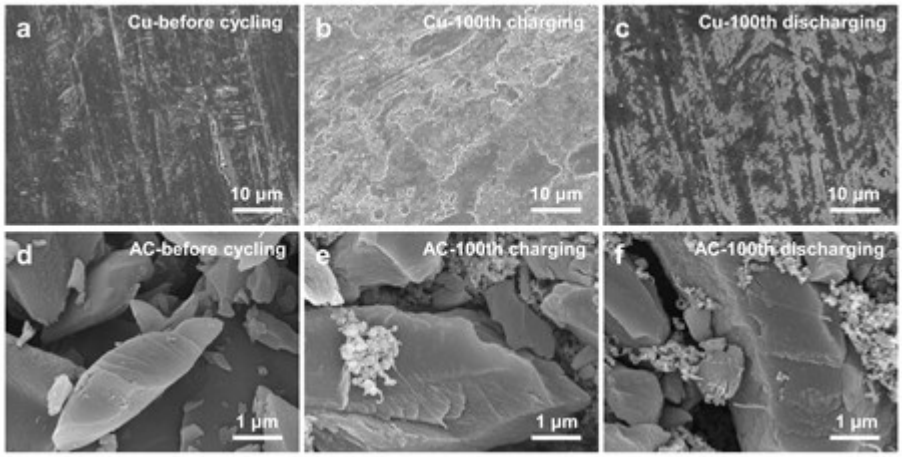

Fig. S30. SEM images of electrodes before and after cycling in Cu||AC batteries at 10 mA cm^{-2}. (a) Cu foil before cycling. (b) Cu foil at the 100th charging state. (c) Cu foil at the 100th discharging state. (d) AC power before cycling. (e) AC cathode at the 100th charging state. (f) AC cathode at the 100th discharging state.

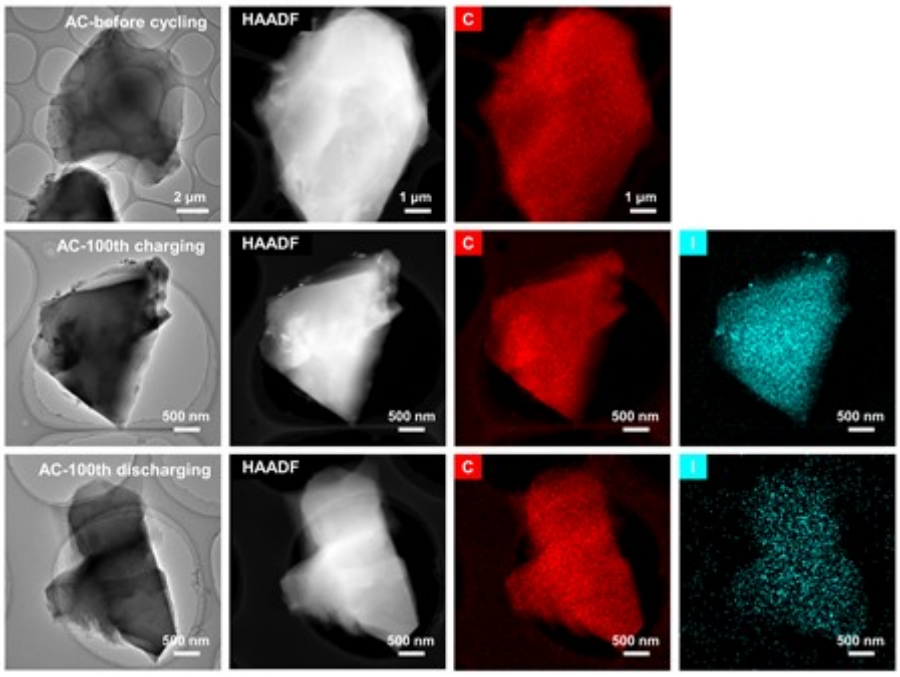

Fig. S31. TEM images, corresponding STEM images, and EDX mapping images of AC before and after cycling in Cu||AC batteries at 10 mA cm^{-2}.

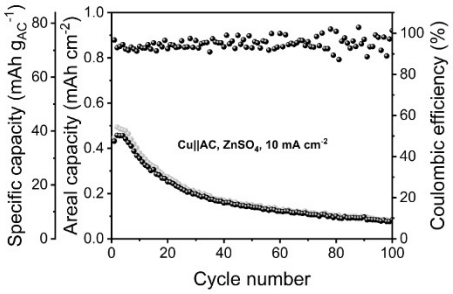

Fig. S32. The electrochemical performance of Cu||AC battery in the $ZnSO_4$ electrolyte.

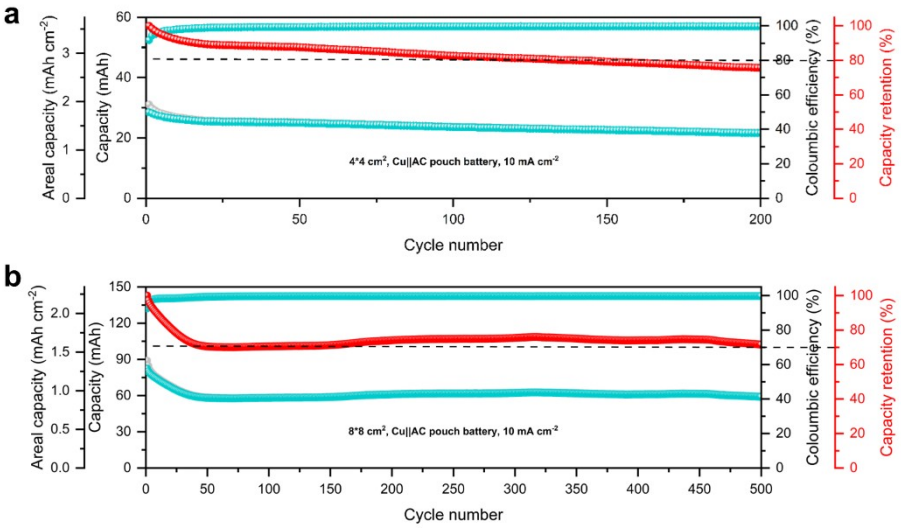

Fig. S33. The electrochemical performance of Cu||AC pouch batteries in the LiI-$ZnSO_4$ electrolyte, (a) 4×4 cm^2, (b) 8×8 cm^2.

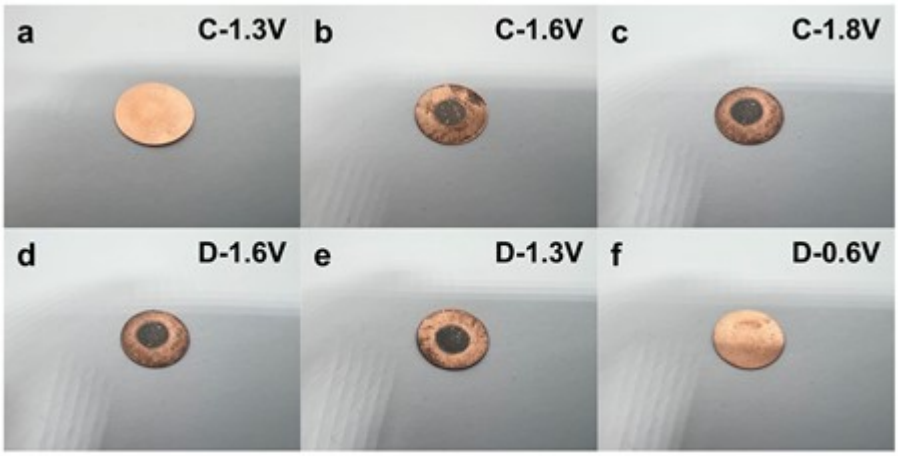

Fig. S34. (a-f) Optical photos of Cu foil in different charging and discharging states in Cu||ACC battery in the LiI-$ZnSO_4$ electrolyte.

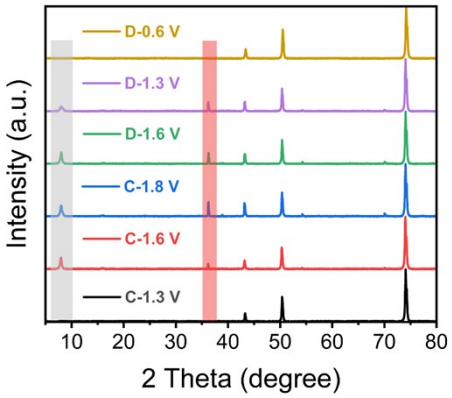

Fig. S35. XRD of Cu foil in different charging and discharging states.

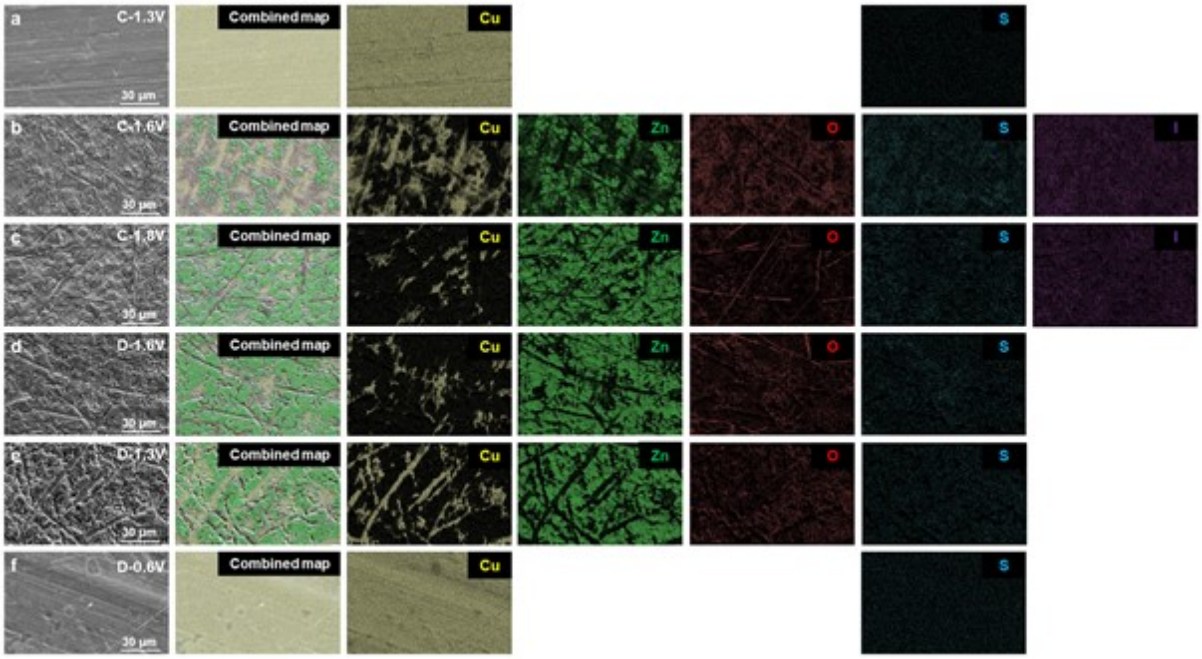

Fig. S36. EDS mapping of Cu foil in different charging and discharging states.

Table S1. Atomic content of element of Cu foil in different charging and discharging states.

SOC \ Element At%	Cu	Zn	O	S	I
C-1.3V	100				
C-1.6V	23.296	33.857	39.649	2.525	0.674
C-1.8V	7.900	54.578	33.235	1.860	2.428
D-1.6V	8.315	54.834	35.674	1.177	
D-1.3V	18.929	56.403	23.842	0.826	
D-0.6V	100.00				

References

1. S. Wang, Y. Zhao, H. Lv, X. Hu, J. He, C. Zhi and H. Li, *Small*, 2023, 2207664.
2. S. Grimme, J. Antony, S. Ehrlich and H. Krieg, *J. Chem. Phys.*, 2010, **132**, 154104-154122.
3. S. Grimme, S. Ehrlich and L. Goerigk, *J Comput Chem*, 2011, **32**, 1456-1465.
4. P. E. Blochl, *Phys. Rev. B*, 1994, **50**, 17953-17979.
5. G. Kresse and D. Joubert, *Phys. Rev. B*, 1999, **59**, 1758-1775.
6. G. Kresse and J. Furthmiiller, *Comput. Mater. Sci.*, 1996, **16**, 15-50.

7. G. Kresse and J. Furthmu¨ller, *Phys. Rev. B*, 1996, **54**, 11169-11186.
8. G. Kresse and J. Hafner, *Phys. Rev. B*, 1994, **49**, 14251-14269.
9. S. F. Nelsen, S. C. Blackstock and Y. Kim, *J. Am. Chem. Soc.*, 1987, **109**, 677-682.
10. F. Wang, H. Hua, D. Wu, J. Li, Y. Xu, X. Nie, Y. Zhuang, J. Zeng and J. Zhao, *ACS Energy Lett.*, 2022, **8**, 780-789.
11. Y. Zhao and D. G. Truhlar, *J. Chem. Phys.*, 2006, **125**, 194101-194118.
12. Q. Deng, S. You, W. Min, Y. Xu, W. Lin, J. Lu and C. Yang, *Adv. Mater.*, 2024, **36**, 2312924.
13. X. Gu, Y. Du, X. Ren, F. Ma, X. Zhang, M. Li, Q. Wang, L. Zhang, C. Lai and S. Zhang, *Adv. Funct. Mater.*, 2024, **34**, 2316541.
14. H. Lu, J. Hu, L. Wang, J. Li, X. Ma, Z. Zhu, H. Li, Y. Zhao, Y. Li, J. Zhao and B. Xu, *Adv. Funct. Mater.*, 2022, **32**, 2112540.
15. Q. Nian, X. Luo, D. Ruan, Y. Li, B. Q. Xiong, Z. Cui, Z. Wang, Q. Dong, J. Fan, J. Jiang, J. Ma, Z. Ma, D. Wang and X. Ren, *Nat. Commun.*, 2024, **15**, 4303.
16. K. Qi, P. Liang, S. Wei, H. Ao, X. Ding, S. Chen, Z. Fan, C. Wang, L. Song, X. Wu, C. Wu and Y. Zhu, *Energy Environ. Sci.*, 2024, **17**, 2566-2575.
17. M. Shi, C. Lei, H. Wang, P. Jiang, C. Xu, W. Yang, X. He and X. Liang, *Angew. Chem. Int. Ed.*, 2024, **63**, e202407261.
18. S. Wang, Z. Huang, J. Zhu, Y. Wang, D. Li, Z. Wei, H. Hong, D. Zhang, Q. Xiong, S. Li, Z. Chen, N. Li and C. Zhi, *Adv. Mater.*, 2024, **36**, 2406451.
19. D. Xie, Y. Sang, D. H. Wang, W. Y. Diao, F. Y. Tao, C. Liu, J. W. Wang, H. Z. Sun, J. P. Zhang and X. L. Wu, *Angew. Chem. Int. Ed.*, 2023, **62**, e202216934.
20. M. Zhang, H. Hua, P. Dai, Z. He, L. Han, P. Tang, J. Yang, P. Lin, Y. Zhang, D. Zhan, J. Chen, Y. Qiao, C. C. Li, J. Zhao and Y. Yang, *Adv. Mater.*, 2023, **35**, 2208630.
21. Y. Zhang, S. Shen, K. Xi, P. Li, Z. Kang, J. Zhao, D. Yin, Y. Su, H. Zhao, G. He and S. Ding, *Angew. Chem. Int. Ed.*, 2024, **63**, e202407067.
22. Z. Zhang, P. Wang, C. Wei, J. Feng, S. Xiong and B. Xi, *Angew. Chem. Int. Ed.*, 2024, **63**, e202402069.